Original Research

Effect of Al_2O_3 Incorporation on the Physicochemical Properties of NiO Thin Films

Asmiet Ramizy, Esam S. Ali*

Department of Physics, College of Science, Anbar University, Al-Anbar, Iraq

Correspondence: esa23s2002@uoanbar.edu.iq

Received: April 9, 2026; Accepted: August 11, 2026

Abstract: Thin films of the spinel compound $NiAl_2O_4$ were synthesized using laser-assisted chemical bath deposition (LACBD). The effect of adding aluminum on the structural and electronic properties of the films was carefully studied. Nickel nitrate hexahydrate [$Ni(NO_3)_2{\cdot}6H_2O$] and aluminum nitrate nonahydrate [$Al(NO_3)_3{\cdot}9H_2O$] were used to fabricate nickel oxide (NiO) and aluminum oxide (Al_2O_3), respectively. The precursor solutions were mixed at different molar concentrations to synthesize thin films of $NiAl_2O_4$. X-ray diffraction (XRD), ultraviolet-visible (UV-Vis) spectroscopy, photoluminescence (PL), field-emission scanning electron microscopy (FESEM), and Raman spectroscopy were conducted to examine the films' structure. XRD analysis indicated that the synthesized $NiAl_2O_4$ films displayed a polycrystalline cubic structure. Using Scherrer's equation, the films' crystallite size was calculated to be 115.5 nm. Optical measurements showed that the films let through about 77.4% of light in the 300-800 nm wavelength range. The optical bandgap was between 3.9 eV and 4.0 eV. FESEM analysis revealed that the average particle size decreased from ≈71 nm to 54 nm with the increase in Al_2O_3 concentration from 0.001 M to 0.01 M. The PL spectrum showed three strong emission peaks at 450, 640, and 850 nm. When aluminum was added, the peak at 640 nm disappeared and the overall intensity dropped. Raman spectroscopy confirmed the formation of the spinel $NiAl_2O_4$ phase through characteristic phonon modes in the range of 200-600 cm^{-1}. Increasing Al_2O_3 incorporation altered local bonding and promoted partial spinel inversion, leading to reduced Raman intensity despite improved crystallinity, as verified by XRD and FESEM.

Keywords: Al_2O_3 Inclusion; NiO Spinel; Laser-Assisted Chemical Bath Deposition; Raman Spectroscopy; Photoluminescence; Optical Characteristics; NiO Thin Films

1. Introduction

Nickel oxide (NiO) is a semitransparent metal oxide semiconductor that works in the visible electromagnetic spectrum, and it has high electrical conductivity and optical transparency[1]. NiO is a well-known p-type oxide semiconductor with a fairly wide indirect bandgap that is usually reported to be between 3.4 eV and 4.0 eV[2,3]. At 26 °C, the lattice constant of NiO is about 4.1769 Å. This material has become the subject of several studies because it exhibits high chemical stability, is inexpensive, and is easy to store. It also has high electrical resistivity, and it is very clear in the visible spectrum. NiO has received considerable attention for different technological uses[2,4], such as light-emitting diodes (LEDs), photodetectors, and supercapacitors, in which it is commonly used as a counter electrode. Metal-oxide NiO films have been widely utilized in various technological applications[5-7]. Sol-gel processing, chemical bath deposition (CBD), hydrothermal synthesis, atomic layer deposition, and radio-frequency (RF) magnetron sputtering are the common techniques used for their fabrication[8-10]. Under appropriate thermal conditions, NiO can react with Al_2O_3 to form the

spinel compound $NiAl_2O_4$[11]. This reaction is facilitated by the structural compatibility between NiO and the spinel lattice, and by the diffusion capability of Ni^{2+} ions within the aluminum matrix[12]. Al_2O_3 is widely recognized as an important material in optical coatings and semiconductor technologies due to its outstanding chemical and physical stabilities[13]. It is characterized by a very low density of structural defects[14], which reduces surface recombination centers[15]. In addition, Al_2O_3 is known to possess a low interface trap density ($D_{it} < 10^{12}$ cm^{-2}) and a high density of negative fixed charges. These features offer efficient field-effect passivation by repelling minority charge carriers away from the surface of the semiconductor to decrease the surface recombination, enhance the carrier lifetime, and increase the photo-response of photodetectors[16-18]. Nickel aluminate ($NiAl_2O_4$) is a spinel oxide that is stable at high temperatures and is made from nickel and aluminum oxides. This material has garnered much attention owing to its high chemical stability, high melting point, and interesting optical properties, making it suitable for use in catalysis, refractory materials, and optoelectronic devices[19]. Aluminate-based materials are commonly used as blue-emitting phosphors in white LEDs due to their high luminescence efficiency, thermal stability, and favorable energy conversion properties[20,21]. Aluminates are also used in plasma display panels and field-emission displays because they give off light well when hit by electrons[22]. They are also used as cathode coatings to enhance the thermal stability and capacity retention[23]. The optical bandgap of these materials usually falls between 3.5 eV and 4.0 eV[24,25]. Even though many studies have been conducted regarding the synthesis and description of NiO and $NiAl_2O_4$ materials, limited research has been performed on the photoluminescence (PL) properties of $NiAl_2O_4$ fabricated through laser-assisted processes. The present study showed how to synthesize the spinel $NiAl_2O_4$ phase through laser-assisted processing without high-temperature heating. The effect of varying concentrations of Al_2O_3 in NiO precursor solutions on the structural and optical characteristics of the resultant films was systematically examined. The PL characteristics of the formed spinel phase were given particular attention. This study aimed to examine the effect of Al_2O_3 incorporation on the structural, optical, and PL properties of NiO-based thin films fabricated via a laser-assisted CBD method.

2. Experimental part

2.1. Preparation of Solutions

Three solutions were prepared as follows: The first solution was obtained by dissolving nickel nitrate hexahydrate [$Ni(NO_3)_2{\cdot}6H_2O$] in deionized water to obtain a 0.05 M solution of NiO. The second solution consisted of NiO at a concentration of 0.05 M and Al_2O_3 at a concentration of 0.001 M, prepared by dissolving aluminum nitrate nonahydrate [$Al(NO_3)_3{\cdot}9H_2O$] in the same manner. The third solution was prepared in the same manner, but with an Al_2O_3 concentration of 0.01 M.

2.2. Thin-Film Preparation

The experimental setup consisted of simple and low-cost equipment, including a glass beaker, a pH meter, a thermometer, a metal stand with clamps to hold the substrates along the inner wall of the beaker, and a burette containing the alkaline solution. The deposition was carried out by laser-assisted chemical bath deposition (LACBD), in which the CBD process was assisted by a continuous-wave blue diode laser with a wavelength of 450 nm and an output power of 5 W. The spot of the laser beam had a diameter of approximately 6.5 cm. The intensity of the irradiation at the substrate surface was measured using a solar irradiance meter, and it was about 500 W/m^2. During the deposition process, the distance between the laser source and the substrate was kept constant at 25 cm. The glass and silicon substrates (1 cm × 1 cm) were vertically dipped into the chemical bath and irradiated with the laser beam vertically incident on their surfaces for 40 min with an energy density of 120 J/cm, as illustrated in **Figure 1**. The deposition process was conducted under continuous stirring using a magnetic stirrer while the solution temperature was increased to 80 °C. The pH of

the solution was maintained at 9 through dropwise addition of ammonium hydroxide by using a burette. After the temperature and pH were stabilized, a glass slide and a silicon wafer were immersed in the bath, and laser irradiation was applied vertically for 40 min. The total deposition time was 60 min. Upon completion, the samples were carefully removed, rinsed with deionized water, and dried at 70 °C. The resulting films were stored for further characterization. For comparison, a pure NiO thin film was synthesized under the same conditions.

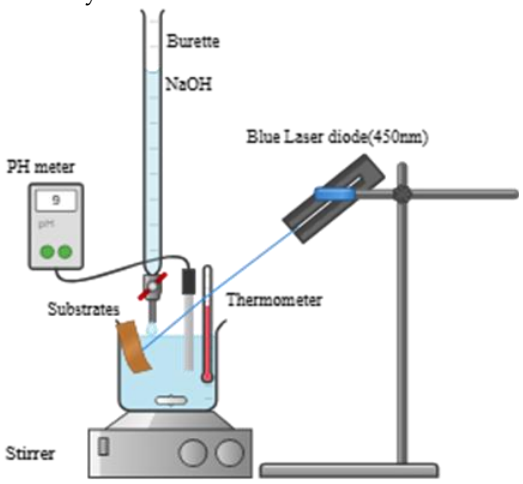

Figure 1. Schematic illustration of the experimental setup used for thin-film deposition by the laser-assisted chemical bath deposition (LACBD) method

3. Result and discussion

3.1. X-ray Diffraction (XRD) Analysis

Figure 2 depicts the XRD patterns of two samples fabricated via LACBD utilizing various mixing ratios of NiO and aluminum oxide with laser assistance. HighScore Plus software was used to determine phases and index peaks with the use of the ICDD-PDF database. The experimental diffraction patterns were well fitted to the standard cubic $NiAl_2O_4$ spinel phase (PDF No. 01-078-0552). The phase identification was based on the combined XRD and Raman analyses. The diffraction peaks seen at 19.08°, 31.40°, 37.01°, 45.01°, 59.91°, 65.55°, and 83.05° corresponded to the (111), (220), (311), (400), (511), (440), and (444) crystallographic planes, respectively. The film fabricated using a lower Al_2O_3 molar concentration (0.001 M) had weak and less defined reflections, especially for the (220), (511), and (444) planes. This finding suggests that the structure was not fully developed, and that the lattice was more disordered. Meanwhile, increasing the Al concentration to 0.01 M resulted in sharper and more intense diffraction peaks.

The as-prepared samples showed diffraction peaks matching to the $NiAl_2O_4$ structure (JCPDS No. 01-078-0552), with distinctive (220), (311), (400), (511), and (440) reflections, according to Salokhe et al.[26]. This study showed that the addition of Al_2O_3 changed the crystal structure in contrast to pure NiO. However, the phase identification was based on the combined evidence from XRD and Raman investigations and was thought to be compatible with the spinel $NiAl_2O_4$ phase in the absence of a reference NiO sample measured under the identical experimental conditions. In contrast, for chemically bath-deposited NiO thin films, distinctive cubic NiO reflections corresponding to the (111), (200), and (220) planes have been recorded[27]. The increased diffraction intensity and reduced broadening of the peaks indicated an increase in the long-range crystallinity of the films with the increase in Al_2O_3 concentration. This improvement can be attributed to the successful addition of Al^{3+} ions to the spinel $NiAl_2O_4$ phase, helping stabilize the lattice, lower the micro-strain, and stop the distortions caused by defects. The crystallite size was estimated using Scherrer's equation ($D = K\lambda/\beta \cos \theta$), where K is the shape factor (0.9), λ is the wavelength of Cu Kα

radiation (1.5406 Å), β is the measured full width at half maximum (FWHM) expressed in radians, and θ is the Bragg angle. The FWHM values were obtained from the XRD peak fitting and converted to radians before the calculation. No correction for instrumental broadening was applied; therefore, the calculated crystallite sizes represent approximate estimates (115.5 nm)[28]. This value suggests the formation of well-developed crystallites with improved structural coherence, which is in line with the increased diffraction peak intensity and reduced peak broadening in the XRD patterns. The variation in crystallite size can be explained by the LACBD process, which usually makes small crystallites because they grow slowly. Meanwhile, laser irradiation adds localized energy that accelerates ion deposition and atomic rearrangement in the crystal lattice. As a result, the crystallinity is enhanced, and the size of the crystallites grows. Furthermore, the high-energy laser accelerates ionic diffusion and encourages cation redistribution in the spinel lattice, helping the spinel $NiAl_2O_4$ phase form and remain stable.

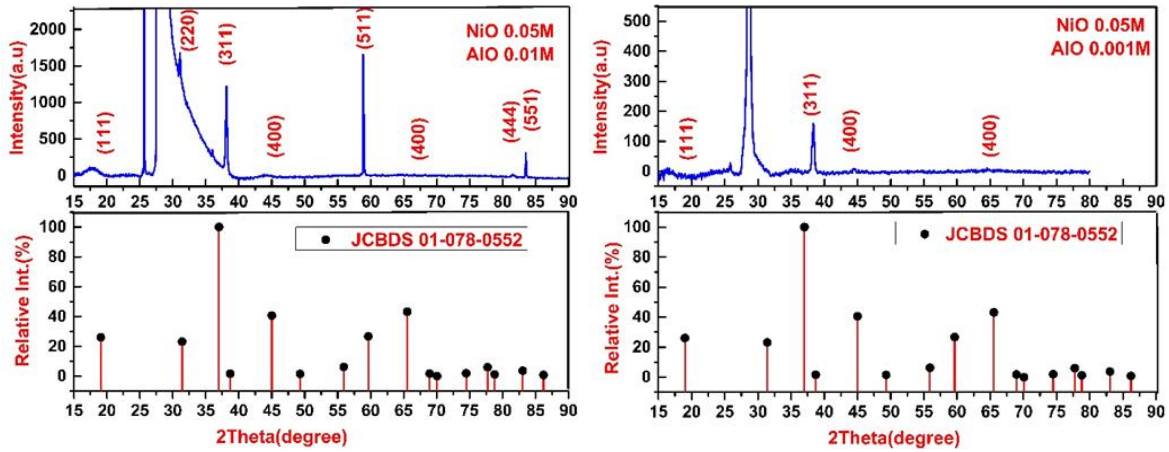

Figure 2. X-ray diffraction (XRD) patterns of $NiAl_2O_4$ thin films deposited using varying aluminum oxide molar concentrations

3.2. UV-Vis Spectral Analysis

Figure 3 displays the transmittance spectra of the three samples fabricated using LACBD. In the spectral range of 300-800 nm, and in comparison with the transmittance in the visible region (400-800 nm), all samples showed a relatively high transmittance of 60%-85%. Comparison of the spectra exhibited that the film prepared using pure NiO (with no Al_2O_3 added) had the lowest transmittance, at 60%. The film with the lowest amount of Al_2O_3 dopant showed a high visible-light transmittance (400-800 nm), reaching about 75%. This value is lower than that of the sample with a high Al_2O_3 concentration, which had a transmittance value of 83%, very close to that of the undoped film. The cross-sectional field-emission scanning electron microscopy (FESEM) images showed that the average thicknesses of the films prepared with 0.001 and 0.01 M Al_2O_3 were about 1.21 μm and 0.560 μm, respectively. The film thickness contributed to the observed transmittance behavior because the optical path length and light absorption depended on it. However, the increased transmittance of the film prepared with 0.01 M Al_2O_3 cannot be simply ascribed to the small reduction in thickness. The transmittance effect of the undoped NiO film thickness was not quantitatively evaluated in the present work because its value was not measured. The XRD results showed that the increased transmittance was associated with the increase in crystallinity and the decrease in structural disorder. Therefore, the optical behavior can be associated with a combined effect of film thickness and microstructural evolution induced by Al_2O_3. Similar observations have been reported in prior studies[29]. Thus, the transmittance differences should be ascribed to the joint effect of the thickness and structural changes, as revealed by Arup Dhara, Sumanta Sain, and others[30,31]. The observed trend aligns with the enhanced structural coherence indicated by XRD and the diminished defect-related emission intensity noted in PL measurements.

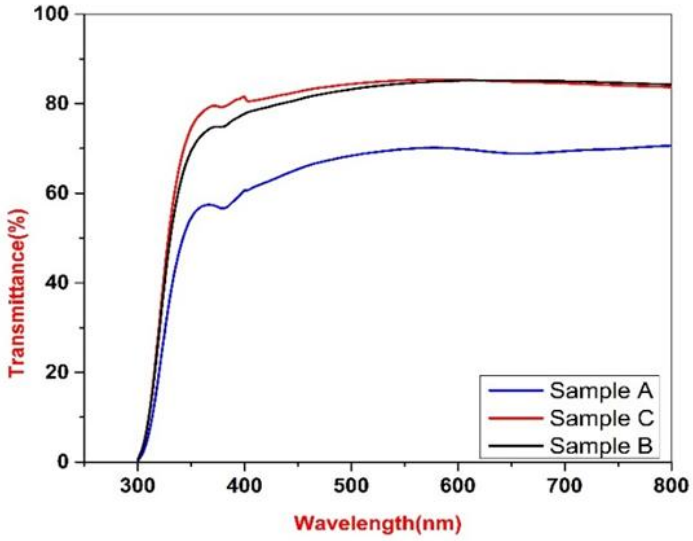

Figure 3. UV-Vis optical transmittance spectra of samples (A), (B), and (C)

Figure 4 shows the optical bandgap energy (E_g) for pure NiO and Al_2O_3-doped NiO thin films at different precursor concentrations (0.001 and 0.01 M). The bandgap values were determined using the Tauc relation $(\alpha h\nu)^n = A(h\nu - E_g)$, where α is the absorption coefficient, $h\nu$ is the photon energy, A is a constant, and E_g is the optical bandgap. In this study, a direct allowed electronic transition was assumed (n = 2). Therefore, the optical bandgap was obtained by plotting $(\alpha h\nu)^2$ versus $h\nu$ and extrapolating the linear portion of the curve to $(\alpha h\nu)^2 = 0$. The pure NiO sample exhibited a bandgap around 3.95 eV[30], and the lowly Al_2O_3-doped sample showed a nearly similar value with a slight decrease. By contrast, the highly doped sample (0.01 M) demonstrated a more pronounced reduction in the bandgap. The small change in the optical bandgap can be attributed to the changes in crystallinity, defect density, and local structural disorder due to the incorporation of Al_2O_3. However, the UV-Vis results are not sufficient to ascertain the precise mechanism, and further compositional characterization or theoretical studies should be performed. These effects lead to subtle changes in the density of states near the band edges, resulting in bandgap narrowing[31]. The estimated bandgap values (≈ 3.9 eV) confirmed that the laser-assisted $NiAl_2O_4$ thin films have a wide bandgap and are suitable for optoelectronic applications that work in the UV range.

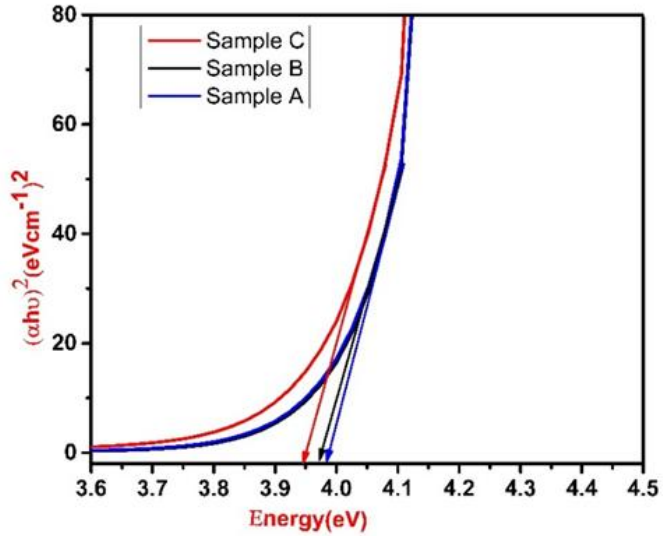

Figure 4. Full-scale Tauc plots of the energy bandgap characteristics of the samples (A), (B), and (C)

3.3. PL Analysis

Figure 5 displays three samples: one sample of pure NiO at a concentration of 0.05 M and the other two samples of NiO doped with varying concentrations of Al_2O_3 (0.001 M and 0.01 M). The pure NiO sample exhibited three strong emission peaks centered at 450, 640, and 825 nm. These emission bands were mostly caused by intrinsic defect states in the bandgap of NiO. The 450 nm emission peak has been generally attributed to the defect states associated with oxygen vacancies of NiO-based materials[32]. These vacancies create localized energy levels within the bandgap that make it easier for photogenerated charge carriers to recombine radiatively. The second emission peak around 640 nm has been widely assigned to the Ni vacancy-related defects in Ni-based oxide materials or the defects on the surface[33]. These defects act as recombination centers for electrons and holes, causing radiative transitions. The third emission in the near-infrared region around 800-830 nm has been attributed to deep defect levels or d-d electronic transitions of Ni^{2+} ions[34]. This phenomenon occurs when the energy levels of Ni^{2+} ions split because of the oxygen ions around them[35], consistent with the findings of Wei et al.[36]. The emission band centered at approximately 650 nm vanished in the NiO films doped with Al_2O_3 at the concentrations of 0.001 M and 0.01 M. The disappearance of this band could be related to the incorporation of Al, which can alter the local defect structure, resulting in modified defect structures and induced lattice distortion; however, the PL results did not provide direct evidence for this mechanism. As a result, changing the energy levels of defects caused the emission peak to shift to the blue end of the spectrum and the peak to spread out further because the structure became more disordered[37]. These findings demonstrated that the incorporation of Al_2O_3 substantially affects the defect structure and optical emission properties of NiO thin films. Moreover, the 825 nm peak noticeably widened and moved to 800 nm while maintaining its strength. Meanwhile, the emission intensity at 450 nm considerably decreased. To the best of the authors' knowledge, comprehensive PL investigations on $NiAl_2O_4$ thin films remain scarce; however, the PL spectrum acquired here resembles that of the spinel $NiFe_2O_4$[38]. The PL emission bands broadened with increasing Al_2O_3 concentration, which can be explained by the wider distribution of localized states of defects and the alteration of the local crystal field caused by Al incorporation. A similar behavior has been observed for NiO- and spinel-based oxides[39]. The presence of Al may further modify the local crystal field around Ni^{2+} ions, thus inducing inhomogeneous broadening of the emission bands. However, the PL results did not provide direct evidence for these mechanisms, and hence, this interpretation should be considered as a plausible explanation[40]. The differences seen in the PL spectra can be linked to the structural results from the XRD analysis. The emergence of the spinel $NiAl_2O_4$ phase following the incorporation of Al_2O_3 indicated a structural alteration of the NiO lattice resulting from the interaction between Al^{3+} ions and Ni^{2+} sites. This change in structure changed how light is emitted, causing the emission band around 650 nm to disappear and the peak near 450 nm to shift to the blue side and widen. These changes indicated an alteration in the defect states and radiative recombination mechanisms related to the formation of the $NiAl_2O_4$ phase.

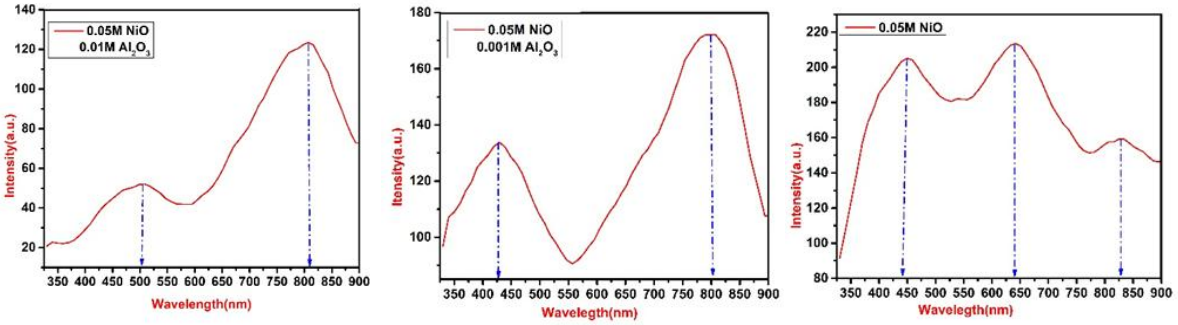

Figure 5. Room temperature photoluminescence (PL) spectra of the prepared thin film samples (A), (B), and (C)

3.4. Raman Spectroscopic Analysis

Previous studies have shown that the Raman spectrum of NiO is composed of first- and second-order phonon modes, and the magnon-related bands are generally observed in the region of 1200-1500 cm^{-1}. Spinel-type aluminates have characteristic Raman-active modes in the region of 300-700 cm^{-1}[40,41]. **Figure 6a** shows the Raman spectra for samples A, B, and C. Peak deconvolution was performed in the low wavenumber region, as shown in **Figure 6b**, to properly identify the Raman-active modes. Three characteristic bands at ≈400, 537, and 686 cm^{-1} were assigned to the E_g, F_{2g}, and A_{1g} vibrational modes of the $NiAl_2O_4$ spinel structure, respectively[42,43]. The E_g mode is related to the symmetric bending vibration of metal-oxygen bonds, and the F_{2g} and A_{1g} modes correspond to metal-oxygen stretching vibrations in the spinel lattice, which confirms the successful formation of the $NiAl_2O_4$ phase. Compared with the Raman modes reported for bulk $NiAl_2O_4$, slight shifts were observed in the peak positions, which may be attributed to nanocrystalline size effects, residual lattice strain, and partial cation redistribution between tetrahedral and octahedral sites induced by laser-assisted CBD[44]. These observations are in agreement with the XRD data, which showed an increase in crystallinity and structural ordering with increasing Al_2O_3 content. In the high wavenumber region (800-1500 cm^{-1}), the second-order phonon and magnon-related bands of NiO (e.g., TO + LO, 2LO, and two-magnon (2M) modes) are shown in **Figure 6c**. Their appearance is a proof of the preservation of the characteristic lattice vibration of the NiO-based matrix[41]. The intensities of the magnon-related bands are similar for all studied samples. The results indicated that Al_2O_3 incorporation did not considerably affect the long-range antiferromagnetic order under the investigated experimental conditions because large changes in the two-magnon Raman band are usually associated with modifications of the antiferromagnetic ordering in NiO[45,46]. Instead, the main spectral changes were observed in the low wavenumber phonon region, where the evolution of the E_g, F_{2g}, and A_{1g} modes is indicative of changes in the local bonding environment and cation distribution upon formation of the $NiAl_2O_4$ spinel[47]. The observed decrease in Raman intensity is more likely to be associated with alterations in local lattice dynamics and cation arrangement induced by Al incorporation than with a reduction in crystallinity, which is consistent with the improved crystallinity observed by XRD[48]. The Raman peak-fitting results showed the characteristic first-order Raman-active modes of the $NiAl_2O_4$ spinel structure at ≈400 (E_g), 537 (F_{2g}), and 686 cm^{-1} (A_{1g}), confirming the phase identification obtained by XRD. The bands at higher wavenumbers (885, 1035, 1165, and 1320 cm^{-1}) are assigned to the TO + LO, 2LO, and 2M modes of NiO, indicating that the Ni-O framework was maintained after Al incorporation. The FWHM values (44-99 cm^{-1}) are indicative of a nanocrystalline structure with residual lattice strain and slight local cation disorder. The similar intensity of the 2M bands suggests that the long-range antiferromagnetic ordering is largely maintained under the present experimental conditions[42]. The detailed peak-fitting parameters, including Raman shift, FWHM, and mode assignment, are listed in **Table 1**.

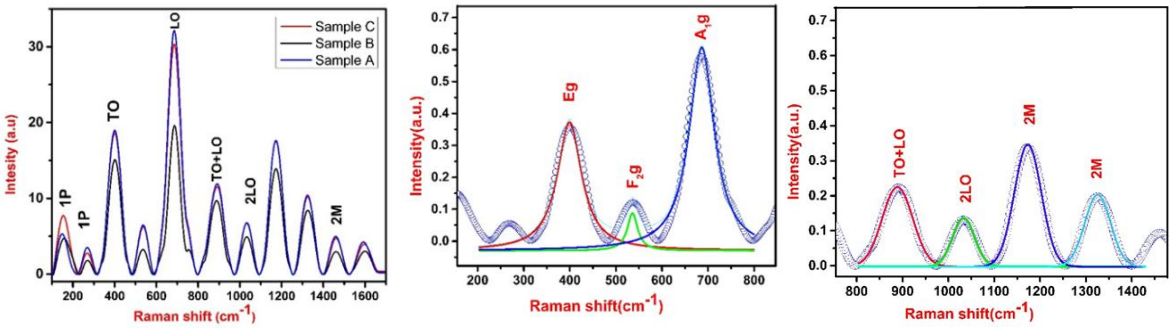

Figure 6. Raman analysis of the prepared thin films: (a) Raman spectra of the samples (A), (B), and (C) at room temperature; (b) Raman peak deconvolution of sample (C) in the 200-800 cm^{-1} range showing the first-order Raman-active phonon modes; and (c) Raman peak deconvolution of sample (C) in the 800-1400 cm^{-1} range showing the second-order phonon and two-magnon scattering modes

Table 1. Peak-fitting results of the Raman spectra showing the Raman shift, FWHM, and assignment of the Raman-active vibrational modes for the thin films containing NiO and Al_2O_3

Raman shift/cm^{-1}	Mode	Assignment	FWHM/cm^{-1}
400	E_g	Symmetric bending	65
537	F_{2g}	Metal-O stretching	44
686	A_{1g}	Al-O symmetric stretching	74
885	TO+LO	Second-order phonon	61
1035	2LO	Second-order LO	99
1165	2M	Two-magnon	60
1320	2M	Two-magnon	83

3.5. FESEM Measurement

The effect of Al_2O_3 concentration on the surface morphology and particle size of the synthesized $NiAl_2O_4$ thin films is shown in **Figure 7** as FESEM micrographs and the corresponding particle-size distribution histograms. Particle-size distribution was analyzed from the FESEM images by using ImageJ software (National Institutes of Health, Bethesda, MD, USA). A total of 101 particles were randomly chosen for each representative sample and measured. The mean particle size and standard deviation were calculated from the measured particle diameters. The prepared film with 0.001 M Al_2O_3 showed comparatively larger particles with conspicuous agglomeration and less uniformity of surface morphology. The corresponding particle-size distribution showed a broader size distribution and an average particle size of (71 ± 34) nm. By contrast, the film prepared with 0.01 M Al_2O_3 presented a more uniform surface made of well-dispersed nanoparticles with lower agglomeration. The particle-size distribution narrowed, and the average particle size was reduced to (54 ± 20) nm. This finding indicated the improved particle-size uniformity with increasing Al_2O_3 concentration. The reduction in particle size demonstrated that the increase in Al_2O_3 concentration affected the growth process of the films, resulting in a smaller and more uniform distribution of the particles. This behavior could be related to a change in the nucleation and growth kinetics during the deposition process. However, the FESEM observations did not directly support an increased nucleation density. Therefore, this interpretation should be considered as a plausible explanation rather than a definitive conclusion. The reduction in particle size reported in [44] is in line with the reduction in crystallite size calculated from the XRD analysis. The cross-sectional FESEM images (**Figure 7c,d**) confirmed the formation of continuous thin films with average thicknesses of (1.21 ± 0.13) and (0.560 ± 0.09) μm for the 0.001 and 0.01 M Al_2O_3 samples, respectively. The decrease in film thickness with increasing Al_2O_3 concentration showed improved nucleation and the formation of a denser and more compact film[49]. This finding demonstrated that the incorporation of Al_2O_3 influenced the microstructure and surface morphology of the deposited films. Therefore, the combined FESEM and XRD results indicated that an increase in Al_2O_3 concentration resulted in the refinement of film microstructure and enhanced uniformity in surface morphology.

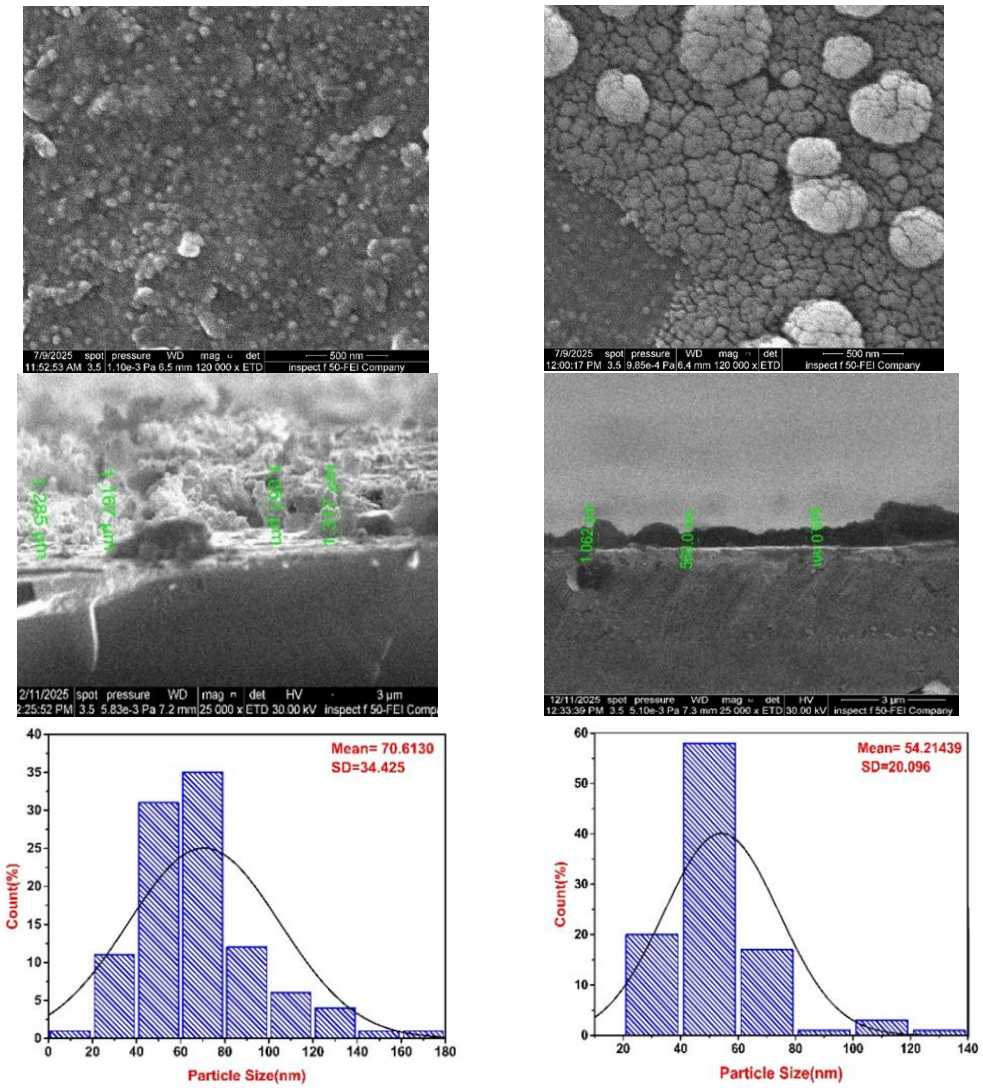

Figure 7. FESEM images of surface and cross-section of the samples (B) and (C): (a) surface morphology of sample (B), (b) surface morphology of sample (C), (c) cross-sectional view of sample (B), (d) cross-sectional view of sample (C), (e) particle size distribution histogram of sample (B), and (f) particle size distribution histogram of sample (C)

4. Conclusion

Thin films were prepared from aqueous precursors of nickel nitrate and aluminum nitrate with various concentrations and mixing ratios using the laser-assisted chemical bath deposition (LACBD) technique. XRD analysis indicated the presence of diffraction peaks related to the characteristic spinel phase of $NiAl_2O_4$. The Raman spectra showed characteristic phonon modes in agreement with the literature values for $NiAl_2O_4$ spinel structures. In combination, the XRD and Raman results indicated the formation of a $NiAl_2O_4$-like spinel structure. Additional compositional characterization is required to conclusively confirm the phase. PL analysis showed that as the concentration of Al_2O_3 increased, defect-related emissions were noticeably suppressed, and the emission peak shifted to the blue side, indicating that the structure became more ordered and the number of defects decreased. FESEM observations and particle-size distribution analysis showed that increasing the amount of aluminum led to the particles being smaller and more uniform in shape. In addition, the optical analysis based on Tauc plots showed a slight variation in the energy bandgap, which can be attributed to the modification of the electronic structure due to Al incorporation and the associated changes in crystallite size and defect states. Overall, the results indicated that aluminum

concentration plays a crucial role in controlling the structural, morphological, and optical properties of $NiAl_2O_4$ nanostructures. Laser-assisted CBD (LACBD) is a good low-temperature method to control the Al_2O_3 concentration for tuning the structural, morphological, and optical properties of $NiAl_2O_4$ thin films. The enhanced crystallinity, low defect density, and tunable optical properties suggest that these films are promising candidates for opto-electronic and photo-responsive device applications. Further confirmation of the cation distribution and phase composition can be obtained by additional compositional analyses such as X-ray photoelectron spectroscopy (XPS) or energy-dispersive X-ray spectroscopy (EDS).

DECLARATIONS

About the Authors

Asmiet Ramizy teaches physics at the University of Anbar's College of Science in Al-Anbar, Iraq. Materials characterisation, optoelectronic devices, and thin-film materials are among his areas of interest.

Esam S. Ali is a researcher at the University of Anbar, Al-Anbar, Iraq's Department of Physics, College of Science. Thin-film materials, optoelectronic materials, laser-assisted deposition, spectroscopy, and photodetectors are among his areas of interest in study.

Author Contributions

Conceptualization: Asmiet Ramizy and Esam S. Ali
Methodology: Esam S. Ali
Data Curation: Esam S. Ali
Formal Analysis: Esam S. Ali
Writing – Original Draft Preparation: Esam S. Ali
Writing – Review & Editing: Asmiet Ramizy and Esam S. Ali
Supervision: Asmiet Ramizy
All authors have read and agreed to the published version of the manuscript.

Acknowledgments

The authors thank the Department of Physics, College of Science, University of Anbar, Iraq for providing laboratory facilities and technical support for this work.

Funding

No funding was received to conduct this research.

Ethics Approval and Consent to Participate

Not applicable

Data Availability Statement

The datasets used and/or analysed during the current investigation are accessible from the corresponding author on reasonable request.

Conflict of Interest

The authors declare that they have no conflict of interest.

AI-Generated Content Declaration

The authors acknowledge the limited use of artificial intelligence (AI)-assisted technology for language editing and improving the clarity and readability of the manuscript. AI assistance was used solely for linguistic refinement and did not contribute to the generation of scientific data, experimental results, data analysis, interpretation of results, or scientific conclusions. The authors remain fully responsible for the accuracy, originality, scientific content, and final version of the manuscript.

References

1. Khurgin, J., Bykov, A. Y. & Zayats, A. V. Hot-electron dynamics in plasmonic nanostructures: fundamentals, applications and overlooked aspects. *eLight* 2024, 4, 15. https://doi.org/10.1186/s43593-024-00070-w
2. Diao, C. C.; Huang, C. Y.; Yang, C. F.; Wu, C. C. Morphological, optical, and electrical properties of p-type nickel oxide thin films by nonvacuum deposition. *Nanomaterials* 2020, 10(4), 636. https://doi.org/10.3390/nano10040636
3. Ibrahim, I. M.; Mohammed, A. S.; Ramizy, A. Responsivity enhancement of lutetium oxide doped-NiO thin films. *Journal of Ovonic Research* 2018, 14(1), 17-25. https://chalcogen.ro/17_MohammedAS.pdf
4. Nayman, E.; Gozukizil, M.F.; Armutci, B.; Temel, S.; Gokmen, F.O. Structural and gas sensing properties of NiO thin films deposited by a novel spin coating technique. *Journal of Sol-Gel Science and Technology* 2025, 114(2), 386-398. https://doi.org/10.1007/s10971-025-06678-9
5. Lucky, S. A.; Sharmin, M.; Das, H.; Podder, J. Evolution in morphological features, enhancement of optical transparency and band gap broadening in manganese-doped nickel oxide thin films for optoelectronics applications. *Thin Solid Films* 2025, 816, 140651. https://doi.org/10.1016/j.tsf.2025.140651
6. Akinkuade, S.; Mwankemwa, B.; Nel, J.; Meyer, W. Structural, optical and electrical characteristics of nickel oxide thin films synthesised through chemical processing method. *Physica B: Condensed Matter* 2018, 535, 24-28. https://doi.org/10.1016/j.physb.2017.06.021
7. Aivalioti, C.; Papadakis, A.; Manidakis, E.; Kayambaki, M.; Androulidaki, M.; Tsagaraki, K.; Pelekanos, N. T.; Stoumpos, C.; Modreanu, M.; Craciun, G.; Romanitan, C.; Aperathitis, E. An assessment of sputtered nitrogen-doped nickel oxide for all-oxide transparent optoelectronic applications: The case of hybrid NiO: N/TiO_2 heterostructure. In *Recent Trends in Chemical and Material Sciences*; Book Publisher International, 2022, 6, 86-111. https://doi.org/10.9734/bpi/rtcams/v6/1650a
8. Napari, M.; Huq, T. N.; Hoye, R. L. Z.; MacManus-Driscoll, J. L. Nickel oxide thin films grown by chemical deposition techniques: Potential and challenges in next-generation rigid and flexible device applications. *InfoMat* 2021, 3(5), 536-576. https://doi.org/10.1002/inf2.12146
9. Miller, M. E. *Nanoporous glass-ceramics for gas separation.* Alfred University, Alfred, NY, USA, 2008.
10. Shih, K. *Stabilization of nickel by aluminum- and iron-rich ceramic materials: Reaction pathways and product leaching behavior.* Stanford University, Stanford, CA, USA, 2005.
11. Vázquez-Fuentes, L. F.; de Oca, A. A. F.; Chavarría-Escamilla, H. G.; Cortés-Jácome, M. A.; Cervantes-Arista, J. I.; Martínez-Ortiz, M. D. J.; López-Salinas, E.; Toledo-Antonio, J. A. Role of Ni/Al molar ratio in Ni-Al mixed oxide catalysts for upgraded vanillin hydrodeoxygenation. *ChemCatChem* 2025, 17(13), e202500222. https://doi.org/10.1002/cctc.202500222
12. Jiong, Y. S. *Physical properties of nickel aluminate spinel and their applications for molten carbonate fuel cell electrodes.* Illinois Institute of Technology, Chicago, IL, USA, 1997.
13. Gu, S.; Lian, H.; Kuang, R.; Lou, B.; Ma, C.; Liu, G.; Wang, J. Laser-driven luminescent ceramic-converted near-infrared II light source for advanced imaging and detection techniques. *Light: Science & Applications* 2025, 14(1), 317. https://doi.org/10.1038/s41377-025-01953-4
14. Kotipalli, R. R. *Surface passivation effects of aluminum oxide on ultra-thin CIGS solar cells.* Université Catholique de Louvain, Louvain-la-Neuve, Belgium, 2016.
15. Dirnstorfer, I.; Simon, D. K.; Jordan, P. M.; Mikolajick, T. Near surface inversion layer recombination in Al_2O_3 passivated n-type silicon. *Journal of Applied Physics* 2014, 116(4), 044112. https://doi.org/10.1063/1.4891021
16. Samikannu, P.; Madhan, V.; Chiang, K. Y.; George, R. K.; Ravi, R. Polylactic acid-based plastic activated $NiAl_2O_4$ nanoparticles as highly active positive electrode materials for energy storage supercapacitor. *Environmental Science and Pollution Research* 2024, 31(18), 26606-26617. https://doi.org/10.1007/s11356-024-32721-3
17. Mohammed, A. S.; Kafi, D. K.; Ramizy, A.; Abdulhadi, O. O.; Hasan, S. F. Nanocrystalline Ce-doped CdO thin films synthesis by spray pyrolysis method for solar cells applications. *Journal of Ovonic Research* 2019, 15(1), 37-42. https://chalcogen.ro/37_MohammedAS.pdf
18. Setälä, O. *Enhanced photodiode performance via surface nanoengineering.* Aalto University, Espoo, Finland, 2025.

19. Zygmuntowicz, J.; Wiecińska, P.; Miazga, A.; Konopka, K. Characterization of composites containing $NiAl_2O_4$ spinel phase from Al_2O_3/NiO and Al_2O_3/Ni systems. *Journal of Thermal Analysis and Calorimetry* 2016, 125(3), 1079-1086. https://doi.org/10.1007/s10973-016-5357-2
20. Zhang, X.; Zhang, J.; Wu, X.; Yu, L.; Liu, Y.; Xu, X.; Lian, S. Discovery of blue-emitting Eu^{2+}-activated sodium aluminate phosphor with high thermal stability via phase segregation. *Chemical Engineering Journal* 2020, 388, 124289. https://doi.org/10.1016/j.cej.2020.124289
21. Srinivas, S.; Vidya, Y. S.; Manjunatha, H. C.; Upendra; Munirathnam, R.; Manjunatha, S.; Vishwalinga Prasad, B.; Shivanna, M.; Suman Kumar. Photoluminescence and supercapacitor potential of eco-friendly synthesized $NiAl_2O_4$ nanoparticles. *Ceramics International* 2025, 51(15), 20395-20402. https://doi.org/10.1016/j.ceramint.2025.02.203
22. David, S. P.; Gaume, R. Electroluminescent thin film phosphors. In *Thin Film Structures in Energy Applications*; Springer: Cham, Switzerland, 2015; pp. 243-269. https://doi.org/10.1007/978-3-319-14774-1_8
23. Kim, M.; Park, J.; Kim, T.; Kang, B.; Im, J.; Jeon, M.; Chae, S.; Ko, M. Morphology control of Al oxide coating to suppress interfacial degradation in ultra-high nickel cathode materials. *Electrochimica Acta* 2025, 517, 145727. https://doi.org/10.1016/j.electacta.2025.145727
24. Kumar, K. V.; Bhavani, S. D. Effect of calcination temperature on structural and optical properties of nickel aluminate nanoparticles. *East European Journal of Physics* 2023, (3), 355-362. https://doi.org/10.26565/2312-4334-2023-3-37
25. Rahman, M. A.; Ahamed, E.; Faruque, M. R. I.; Islam, M.T. Preparation of $NiAl_2O_4$-based flexible substrates for metamaterials with negative dielectric properties. *Scientific Reports* 2018, 8(1), 14948. https://doi.org/10.1038/s41598-018-33295-0
26. Salokhe, P.; Shetti, S.; Patil, V.; Patil, T.; Nille, R.; Chougale, A.; Gurav, K.; Sutar, R.; Jatratkar, A.; Chougale, G.; Yadav, J.; Mohite, B.; Bargir, S.; Patil, R. B.; Tamboli, S. H. Study of physical properties of chemical bath deposited nickel oxide thin films. Materials Today: *Proceedings* 2021, 43, 2810-2813. https://doi.org/10.1016/j.matpr.2020.09.328
27. Solanki, K. D.; Tanna, A. R.; Desai, H. B. Photocatalytic degradation of various dyes using spinel aluminates and their composites: A review. *EPJ Web of Conferences* 2026, 348, 03005. https://doi.org/10.1051/epjconf/202634803005
28. Ramay, S. M.; Siddiqi, S. A.; Atiq, S.; Awan, M. S.; Riaz, S. Structural, magnetic, and electrical properties of Al^{3+} substituted CuZn-ferrites. *Chinese Journal of Chemical Physics* 2010, 23(5), 591-595. https://doi.org/10.1088/1674-0068/23/05/591-595
29. Owoeye, V. A.; Adewinbi, S. A.; Salau, A. O.; Orelusi, A. N.; Adeoye, A.E.; Akindadelo, A. T. Effect of precursor concentration on stoichiometry and optical properties of spray pyrolyzed nanostructured NiO thin films. *Heliyon* 2023, 9(1), e13023. https://doi.org/10.1016/j.heliyon.2023.e13023
30. Dhara, A.; Sain, S.; Ray, A.; Das, S.; Pradhan, S. K. Microstructure analysis, optical, and electrical transport properties of $NiAl_2O_4$/Al_2O_3 nanocomposite powder. *Physica Status Solidi (A)* 2022, 219(22), 2200386. https://doi.org/10.1002/pssa.202200386
31. Ivanova, T.; Harizanova, A.; Petkov, N. Optical, electrical, and structural properties of NiO thin films derived by sol-gel method. *Gels* 2025, 11(12), 944. https://doi.org/10.3390/gels11120944
32. Geetha, V. T.; Selvakumar, C.; Hema, K.; Selvarani, V.; Kumutha, P. Tuning the catalytic activity of NiO via neodymium doping for selective benzaldehyde formation. *Journal of Inorganic and Organometallic Polymers and Materials* 2026, 1-12. https://doi.org/10.1007/s10904-026-04273-1
33. Monica, S. E. S.; Dhas, C. R.; Venkatesh, R.; Sivakumar, R.; Vignesh, R.; Ferby, V. A. Nebulizer sprayed nickel-manganese (Ni-Mn) mixed metal oxide nanocomposite coatings for high-performance electrochromic device applications. *Journal of Solid State Electrochemistry* 2022, 26(5), 1271-1290. https://doi.org/10.1007/s10008-022-05159-1
34. Wang, Y.; Ran, C.; Huang, C.; Wu, F.; Li, J.; Zhang, Q.; Teng, Y.; Xie, X.; Dong, H.; Mu, Z. Simultaneously enhancing the near infrared emission intensity and improving the luminescence thermal stability via fluorination strategy in Ni^{2+} doped germanates. *Ceramics International* 2025, 51(27), 54758-54766. https://doi.org/10.1016/j.ceramint.2025.09.202
35. Mohseni Meybodi, S.; Hosseini, S.; Rezaee, M.; Sadrnezhaad, S.; Mohammadyani, D. Synthesis of wide band gap nanocrystalline NiO powder via a sonochemical method. *Ultrasonics Sonochemistry* 2012, 19(4), 841-845. https://doi.org/10.1016/j.ultsonch.2011.11.017

36. Wei, H.; Wu, Y. Study on the up-conversion luminescence and conductivity behavior of p-type NiO:Yb,Er thin films. *Materials* 2023, 16(13), 4637. https://doi.org/10.3390/ma16134637
37. Allali, M.; Dahamni, M.A.; Ghamnia, M.; Boukhachem, A.; Boukrédimi, D.; Tonneau, D.; Fauquet, C. Synthesis and investigation of pure and Cu-doped NiO nanofilms for future applications in wastewater treatment rejected by textile industry. *Catalysts* 2022, 12(9), 931. https://doi.org/10.3390/catal12090931
38. Khani, Y.; Pyo, S.; Bahadoran, F.; Cho, K.; Jeong, K.; Park, Y. Synthesis of coke-resistant catalyst using $NiAl_2O_4$ support for hydrogen production via autothermal dry reforming of methane. *ChemCatChem* 2025, 17(1), e202401015. https://doi.org/10.1002/cctc.202401015
39. Wahba, M. A. Recent developments in metal oxide semiconductor photocatalysts for solar-driven environmental applications. *Discover Materials* 2026, 6(1), 127. https://doi.org/10.1007/s43939-026-00585-8
40. Derkaoui, K.; Bencherifa, I.; Elfiad, A.; Boukhouidem, K.; Kechouane, M.; Mebdoua, Y.; Hadjersi, T. Nickel aluminate spinel as a noble-metal-free electrocatalyst for alkaline hydrogen evolution reaction. *Reaction Kinetics, Mechanisms and Catalysis* 2026, 139(3), 2349-2369. https://doi.org/10.1007/s11144-026-03080-6
41. Bala, N.; Singh, H. K.; Verma, S.; Rath, S. Magnetic-order induced effects in nanocrystalline NiO probed by Raman spectroscopy. *Physical Review B* 2020, 102(2), 024423. https://doi.org/10.1103/PhysRevB.102.024423
42. Laguna-Bercero, M. A.; Sanjuán, M. L.; Merino, R. I. Raman spectroscopic study of cation disorder in poly- and single crystals of the nickel aluminate spinel. *Journal of Physics: Condensed Matter* 2007, 19(18), 186217. https://doi.org/10.1088/0953-8984/19/18/186217
43. Ali, M. I.; Sivanandakrishnan, A.; Jacob, S.; Gopakumar, G.; Patra, M. K.; Janu, Y.; Chauhan, V. S.; Hussain, S.; Ali, M. S.; Hazra, S. Carbon-encapsulated $NiAl_2O_4$ spinel nanocomposites for bifunctional hydrogen evolution and high-performance supercapacitors. *Journal of Materials Science* 2026, 61(28), 20256-20274. https://doi.org/10.1007/s10853-026-13063-6
44. Zhou, K.; Wu, S.; Zhou, Y.; Zhang, Y.; Lei, X.; Wang, X.; Xu, X.; Gong, W.; Li, Y.; Wang, Z. Al-induced unusual grain growth in Ni-Co-Cr multi-principal element alloys. *Materials* 2026, 19(3), 505. https://doi.org/10.3390/ma19030505
45. Funkenbusch, E.; Cornilsen, B. Two-magnon Raman scattering in calcium doped NiO. *Solid State Communications* 1981, 40(6), 707-710. https://doi.org/10.1016/0038-1098(81)90624-4
46. Qiu, J.; Nguyen, T. H.; Lee, Y. J.; Kim, S.; Kim, S.; Kim, S. J.; Song, M. T.; Huang, W. J.; Chen, X. B.; Yang, I. S. Strong oxygen-content dependence of the magnetic excitations in antiferromagnetic NiO nanoparticles: A Raman probe. *Spectrochimica Acta Part A: Molecular and Biomolecular Spectroscopy* 2023, 297, 122700. https://doi.org/10.1016/j.saa.2023.122700
47. Lamichhane, S. *Electronic and magnetic properties of ordered and disordered binary alloy Ni-Al*. Tribhuvan University, Kathmandu, Nepal, 2019.
48. Farhan, M. A.; Javaid, S.; Rasheed, L.; Ur Rehman, M. A.; Nadeem, M. Tunability of domain structure in partially inverse spinels $NiAl_2O_4$. *Heliyon* 2024, 10(9), e30181. https://doi.org/10.1016/j.heliyon.2024.e30181
49. Hodes, G. *Chemical Solution Deposition of Semiconductor Films*; Marcel Dekker: New York, NY, USA, 2002.